

Estimating parameters of the nonlinear cloud and rain equation from a large-eddy simulation

Lunderman, Spencer; Morzfeld, Matthias; Glassmeier, Franziska; Feingold, Graham

DOI

[10.1016/j.physd.2020.132500](https://doi.org/10.1016/j.physd.2020.132500)

Publication date

2020

Document Version

Accepted author manuscript

Published in

Physica D: Nonlinear Phenomena

Citation (APA)

Lunderman, S., Morzfeld, M., Glassmeier, F., & Feingold, G. (2020). Estimating parameters of the nonlinear cloud and rain equation from a large-eddy simulation. *Physica D: Nonlinear Phenomena*, 410, Article 132500. <https://doi.org/10.1016/j.physd.2020.132500>

Important note

To cite this publication, please use the final published version (if applicable). Please check the document version above.

Copyright

Other than for strictly personal use, it is not permitted to download, forward or distribute the text or part of it, without the consent of the author(s) and/or copyright holder(s), unless the work is under an open content license such as Creative Commons.

Takedown policy

Please contact us and provide details if you believe this document breaches copyrights. We will remove access to the work immediately and investigate your claim.

Estimating parameters of the nonlinear cloud and rain equation from a large-eddy simulation

Spencer Lunderman^a, Matthias Morzfeld^b, Franziska Glassmeier^{c,d,e}, and Graham Feingold^d

^aDepartment of Mathematics, University of Arizona

^bInstitute of Geophysics and Planetary Physics, Scripps Institution of Oceanography,
University of California, San Diego

^cDepartment of Environmental Sciences, Wageningen University

^dChemical Sciences Laboratory/Earth System Research Laboratories, NOAA

^eCurrently at: Faculty of Civil Engineering and Geosciences Department of Geoscience and
Remote Sensing, Delft University of Technology.

April 10, 2020

Abstract

Predator-prey dynamics have been suggested as simplified models of stratocumulus clouds, with rain acting as a predator of the clouds. We describe a mathematical and computational framework for estimating the parameters of a simplified model from a large eddy simulation (LES). In our method, we extract cycles of cloud growth and decay from the LES and then search for parameters of the simplified model that lead to similar cycles. We implement our method via Markov chain Monte Carlo. Required error models are constructed based on variations of the LES cloud cycles. This computational framework allows us to test the robustness of our overall approach and various assumptions, which is essential for the simplified model to be useful. Our main conclusion is that it is indeed possible to calibrate a predator-prey model so that it becomes a reliable, robust, but simplified representation of selected aspects of a LES. In the future, such models may then be used as a quantitative tool for investigating important questions in cloud microphysics.

Keywords

Predator-prey dynamics; Large-eddy simulation; Stratocumulus clouds; Bayesian inversion; Markov chain Monte Carlo;

1 Introduction

Stratocumulus cloud decks can reach 1000s of km in scale and cover vast stretches of the subtropical oceans. These decks consist of a space-filling arrangement of convective cells, with clouds marking updraft regions. Depending on the environmental conditions like sea-surface temperature or atmospheric aerosol, stratocumulus occur in two configurations (Agee, 1984; Wood and Hartmann, 2006; Glassmeier and Feingold, 2017)

- (i) wide updraft areas coinciding with cloud cells (“closed-cells”) whose *cloud-free boundaries* form a honeycomb-like pattern;
- (ii) narrow updrafts and cloudy rings that outline a honeycomb-like pattern (“open cells”).

37 Due to its lower cloud fraction, the open-cell configuration is significantly less reflective than the
38 closed-cell configuration. Since roughly one fifth of the Earth’s surface is covered by stratocumulus
39 cloud decks (Wood, 2012), the radiative effects of stratocumulus have a large impact on the Earth’s
40 energy budget. In fact, stratocumulus remain one of the main sources of uncertainty in quantifying
41 climate change (Boucher et al., 2013; Myhre et al., 2013; Schneider et al., 2017).

42 Stratocumulus, and in particular transitions from closed-cell to open-cell configurations, have
43 been studied numerically with a hierarchy of mathematical and computational models. Large eddy
44 simulations (LES) resolve the governing equations of moist hydrodynamics down to the cloud scale
45 and can faithfully represent the formation of stratocumulus and how they transition between the
46 open- and the closed-cell configurations, see, e.g., Feingold et al. (2015). In addition to these
47 detailed but computationally expensive models, drastically simplified, low-dimensional models have
48 been proposed to capture the spatial configuration of stratocumulus. For example, dynamic cellular
49 networks can be used to describe the patterns that are formed within stratocumulus cloud systems
50 (Glassmeier and Feingold, 2017). Predator-prey models, where the rain acts as the predator of
51 clouds, have been proposed as phenomenological models for stratocumulus (Koren and Feingold,
52 2011; Feingold and Koren, 2013; Koren et al., 2017).

53 The predator-prey models can reproduce two configurations that are relevant to stratocumulus
54 clouds: oscillatory (limit cycle) and stationary solutions for cloud depth. The limit cycles model a
55 scenario in which strong rain dissipates the cloud that created it, followed by renewed cloud build-up
56 that proceeds until the cloud is again thick enough to produce strong rain, which restarts the whole
57 process. A stationary cloud depth represents a situation in which the rain consumes the cloud at
58 the same rate as the cloud replenishes.

59 We focus on one of the predator-prey models, the nonlinear cloud and rain equation of Koren
60 et al. (2017), which we call KTF17 for short. Our primary goal is to build a mathematical and
61 computational framework to convert KTF17 into a quantitative tool. We argue that this can be
62 done by adopting a Bayesian approach, in which a posterior distribution over the parameters of
63 KTF17 is defined based on cloud depth time series of stratocumulus. A natural data source for
64 these time series would be observations of stratocumulus in the Earth’s atmosphere, e.g., derived
65 from the Geostationary Operational Environmental Satellite-R Series (GOES-R). KTF17 does not
66 account for horizontal advection which is usually present in satellite derived observations. Using
67 observational data would thus require tracking stratocumulus patches within a larger cloud system
68 over time to “remove” advection, see, e.g., Koren and Feingold (2013). To avoid these technicalities,
69 we use LES output, generated in the absence of advection, as “data” in place of observations. The
70 resulting KTF17 model, with stochastic parameters distributed according to a posterior distribution,
71 is thus a quantitative, but simplified representation of selected aspects of cloud systems that are
72 realistically represented by LES. Our approach thus connects the extreme ends of the hierarchy of
73 cloud models and may be used to obtain new insights into complex cloud and rain interactions. Given
74 the example of the predator-prey-based parameterization of Nuber and Graf (2005) to represent
75 convection, simple predator-prey models, “calibrated” to a LES via a parameter estimation, may
76 eventually even prove useful for representing some aspects of cloud systems in climate models. We
77 focus, however, on establishing a suitable mathematical and computational framework for the task
78 of “calibrating” a predator-prey model with LES data.

79 More specifically, we describe how parameters of KTF17 can be estimated from a LES by
80 a “Bayesian inversion”. The inversion is based on two distributions: a prior distribution, that
81 represents knowledge about the model parameters, *without* taking the data into account, and a
82 likelihood, that describes the probability of the data, given a set of parameters, see, e.g., Reich
83 and Cotter (2015); Asch et al. (2017); Tarantola (2005). Jointly, the prior and likelihood define
84 a posterior distribution over the parameters that represents our knowledge of the parameters and

85 their uncertainties in view of the data, our prior knowledge and assumed errors.

86 Typically, a likelihood is based on a point-wise mismatch of model outputs and data. In our
87 context, the “data” are a time series of cloud depth of the LES, i.e., a 2D field that evolves over
88 time (note that we refer to simulation outputs as data because we treat them as such). KTF17,
89 however, does not have an associated spatial scale. Thus, it is not straightforward to compare
90 KTF17 to LES output. We address this issue by using “feature-based” likelihoods (Maclean et al.,
91 2017; Morzfeld et al., 2018). The basic idea is that compressing the data into suitable features
92 can bridge gaps between drastically simplified models and complex processes. The feature we
93 consider is a stochastic representation of cycles of growth and decay in cloud depth, derived from
94 the LES, that can be compared directly (point-wise) to limit cycles of KTF17. Required error
95 models of the features are constructed based on variations of the cloud cycles extracted from the
96 LES. We solve the resulting, feature-based inverse problem numerically by a Markov chain Monte
97 Carlo (MCMC) method. This means that we generate a (large) set of physically relevant “samples”
98 (model parameters) that lead to KTF17 limit cycles that are comparable to the cloud cycles observed
99 in the LES, to within the assumed errors. In particular, we observe an overall good fit in terms of
100 the cycle’s periods, amplitudes and average growth and decay times. The Bayesian approach and
101 MCMC implementation further provide information about posterior errors and uncertainties, which
102 in turn depend on expected model errors. This allows us to assess, in hindsight, the validity of our
103 assumptions about errors and error models. We further carefully test the robustness of our overall
104 approach by numerical sensitivity studies. These tests of robustness and of the validity of error
105 models are essential to being able to use KTF17 to make precise and definite statements. Finally,
106 we illustrate how to use our technique to investigate cloud microphysics questions. Specifically,
107 we compute sensitivity of model parameters to temporal changes in the morphology of the cloud
108 system. We must emphasize that our results and conclusions with respect to cloud microphysics
109 are limited, in part because our study is limited to one particular LES.

110 **2 Background: the nonlinear cloud and rain equation, the LES and** 111 **feature-based Bayesian inversion**

112 We use a Bayesian approach to combine information from a LES with a simplified predator-prey
113 model of stratocumulus clouds. In this section, we describe the predator-prey model and the LES.
114 We then provide background and notation for Bayesian inversion and feature-based Bayesian inver-
115 sion.

116 **2.1 The nonlinear cloud and rain equation (KTF17)**

117 The coevolution of cloud and rain can be captured, qualitatively, by predator-prey type dynamics
118 and, more specifically, by differential equations with a delayed sink term (Koren and Feingold, 2011;
119 Feingold and Koren, 2013; Koren et al., 2017). The delay stems from the fact that the predator
120 (rain) is produced by the cloud (prey) with a delay that is associated with the time required for
121 cloud droplets to coalesce to form larger raindrops. This delay time is a function of the amount of
122 cloud water and the cloud drop concentration and is typically on the order of 15 minutes.

123 The predator-prey models are capable of reproducing two different dynamical regimes that are
124 relevant to stratocumulus clouds. When the predator-prey models exhibit a constant cloud depth,
125 the rain consumes the cloud at the same rate as cloud replenishment. When the predator-prey
126 models exhibit oscillations (limit cycles), strong rain nearly depletes the cloud and then dissipates
127 until the cloud is thick enough to again produce rain.

128 We consider the “nonlinear cloud and rain equation” (Koren et al., 2017), subsequently called
 129 KTF17:

$$\frac{dH}{dt} = \frac{H_0 - H}{\tau} - \frac{\alpha}{\sqrt{N}} H^2 (t - T). \quad (1)$$

130 Here, H (in m) is cloud depth, H_0 (in m) is the cloud depth carrying capacity, τ (in days) is the
 131 characteristic time to reach carrying capacity, T (in days) is the delay associated with the time
 132 it takes to generate rain and N (in cm^{-3}) is the droplet concentration; the scaling factor α (in
 133 $\text{day}^{-1}\text{m}^{-2.5}$) links the cloud depth, droplet concentration and rain rate (see Koren et al. (2017) for
 134 further detail).

135 In summary, the parameters of the KTF17 model are the delay, the carrying capacity, the
 136 characteristic time and the scaling factor. For a given set of parameters and initial conditions,
 137 we solve (1) numerically by a 4th order Runge-Kutta method with time step $\Delta t = 0.1$ min. The
 138 numerical integration requires that we prescribe the cloud depth $H(t)$ during “negative times” on
 139 the interval $t \in [-T, 0]$ and we assume that $H(t)$ is constant during this interval. The result of a
 140 numerical solution of KTF17 is a time series of cloud depth.

141 We note that KTF17 assumes that droplet concentration be fixed. This is justified when there
 142 is an approximate balance between replenishment of aerosol particles, which form the nuclei for new
 143 droplets, and consumption of droplets/particles via coalescence and their removal by rain. Below,
 144 we use values between $N = 16 \text{ cm}^{-3}$ and $N = 45 \text{ cm}^{-3}$, which are typical of the drop concentrations
 145 in clean marine environments associated with open cellular convection and which are also in line
 146 with the values of N in the LES we consider (see Section 2.2). Nonetheless, droplet concentration
 147 may not be constant in a stratocumulus cloud system or in an LES ((Yamaguchi et al., 2017)). Thus,
 148 the fixed droplet concentration may limit the usefulness of the KTF17 model in certain conditions.
 149 We discuss these issues in more detail below.

150 2.2 Description of the LES

151 A LES is a detailed model of a cloud system in space (3D) and time. It solves the anelastic
 152 Navier–Stokes equations on an Eulerian spatial grid, resolving convection and clouds, and in the
 153 current work, also simulates microphysical processes such as the formation of droplets on suspended
 154 particles (condensation nuclei), their growth by coalescence, and their removal by rain. We use the
 155 LES output to estimate the parameters of KTF17, which produces a times series of cloud depth (H
 156 in (1)). During Bayesian inversion, we will connect KTF17 to the LES by extracting time series of
 157 cloud depth from the LES (see Section 3.2).

158 We use the LES described in Feingold et al. (2015), with modifications. The atmospheric
 159 conditions derive from a well studied drizzling stratocumulus case, but unlike Feingold et al. (2015),
 160 the initial concentration of particles on which drops can form is about 100 cm^{-3} but decreases
 161 naturally due to droplet coalescence and rain removal processes.

162 The spatial domain of the LES is 40 km by 40 km wide and 1.6 km high with a grid spacing
 163 of 200 m in the horizontal and 10 m in the vertical. The simulation covers a total of 12 hrs with
 164 a time step of one second. Simulation output is available every one minute. We disregard the first
 165 4.5 hours of the LES during which the system rapidly transitions from a closed-cell to an open-cell
 166 state. We thus only consider 7.5 hours, or 450 minutes, of simulation of an open-cell system for the
 167 Bayesian inversion.

168 The KTF17 model describes cloud depth as a function of time, but not any other quantities
 169 of the LES. For this reason, we consider cloud depth of the LES and disregard most other simu-
 170 lation outputs with the exception of droplet concentration N and column liquid water path, (see

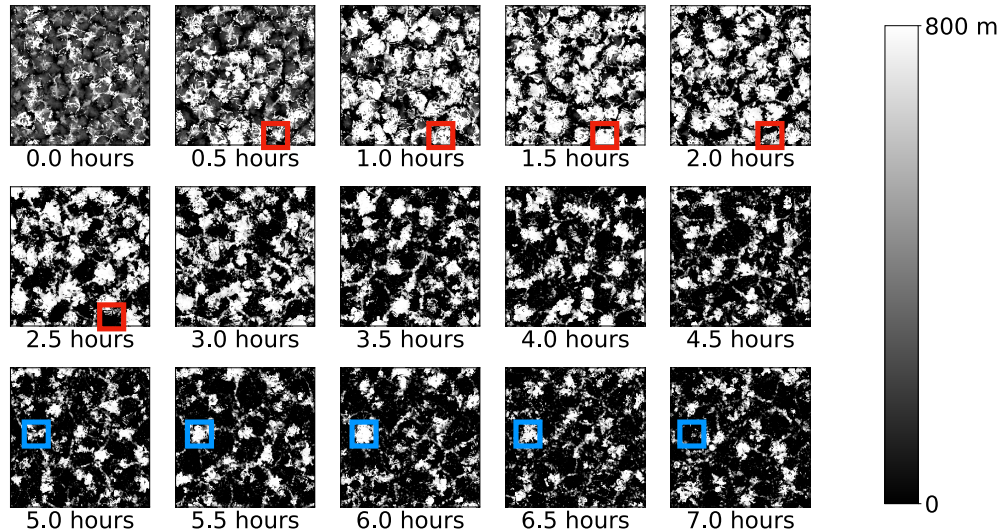


Figure 1: Snapshots, taken every 30 mins, of the 2D cloud depth field of the LES. Examples of cloud cycles, i.e., an increase in cloud depth, followed by a decrease in cloud depth, are highlighted by blue and red squares. After Feingold et al. (2015).

171 Section 3.2). Figure 1 shows snapshots of the cloud depth field over the span of 7 hrs, sampled
 172 every 30 minutes, which is approximately the decorrelation timescale of the cloud field.

173 Figure 1 illustrates that, during the first 3.5 hrs, the system is characterized by a relatively dense
 174 collection of clouds with high average cloud fraction; a gradual transition to a lower cloud fraction
 175 then occurs as the cloud system self-organizes into a sparse collection of cloudy rings that outline
 176 a honeycomb-like pattern of cloud-free cells. We will refer to the first 3.5 hrs of simulation as the
 177 “dense phase” and to the remaining 4 hrs of simulation as the “sparse phase” (see Section 4.2). The
 178 droplet concentration falls from about 45 cm^{-3} down to 16 cm^{-3} during the course of the 7.5 hrs
 179 of simulation, as illustrated in Figure 2. We compute the droplet concentration over cloudy parts
 180 of the domain by averaging N vertically and horizontally over the entire domain and scale this
 181 average by the average cloud fraction. The consequences for parameter estimation with KTF17,
 182 which assumes a constant N , will be discussed in detail below.

183 2.3 Bayesian inversion

184 Bayesian inversion means inferring information about model parameters from data. This is done
 185 as follows. We denote the model parameters by the vector $\boldsymbol{\theta}$ and we write the model as $\mathcal{M}(\boldsymbol{\theta})$.
 186 The function \mathcal{M} could, for example, involve solving the KTF17 model numerically to produce time
 187 series of cloud depth (see below). A priori, one may know a few things about the parameters. For
 188 example, one may know that certain parameters must be positive to be physically relevant. In the
 189 Bayesian framework, such “prior knowledge” is expressed as a prior distribution $p_0(\boldsymbol{\theta})$. Priors are
 190 often uniform distributions. For example, if bounds on the parameters are known, then the prior
 191 can be chosen uniformly within the bounds.

192 For a given $\boldsymbol{\theta}$, the numerical model can be simulated and its output can be compared to data,
 193 \mathbf{y} . Model and data are thus connected by

$$\mathbf{y} = \mathcal{M}(\boldsymbol{\theta}) + \boldsymbol{\eta}, \quad (2)$$

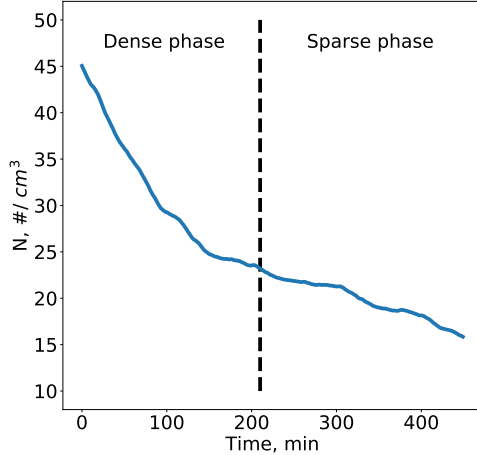


Figure 2: Droplet concentration N , scaled by average cloud cover, as a function of time. The dashed vertical line indicates the separation of the dense and sparse phases of the simulation

194 where $\boldsymbol{\eta}$ represents discrepancies between the model and data, and is typically assumed to be
 195 Gaussian distributed with mean zero and covariance matrix \mathbf{R} . Equation (2) then defines the
 196 “likelihood”

$$p_l(\mathbf{y}|\boldsymbol{\theta}) \propto \exp\left(-\frac{1}{2}\|\mathbf{R}^{-1/2}(\mathbf{y} - \mathcal{M}(\boldsymbol{\theta}))\|^2\right), \quad (3)$$

197 where $\mathbf{R}^{1/2}$ is a matrix square root and where the vertical bars denote the Euclidean norm. The
 198 prior and likelihood jointly define the posterior distribution

$$p(\boldsymbol{\theta}|\mathbf{y}) \propto p_0(\boldsymbol{\theta}) p_l(\mathbf{y}|\boldsymbol{\theta}), \quad (4)$$

199 which describes our knowledge of the parameters and their uncertainties in view of the data. This
 200 means, in particular, that a numerical model with parameters distributed according to the poste-
 201 rior distribution, is “calibrated” to the data in the sense that simulations lead to model outputs
 202 compatible with the data up to the assumed errors.

203 2.4 Feature-based Bayesian inversion

204 In many Bayesian inverse problems, the model \mathcal{M} is an accurate and detailed representation of
 205 the physical process that generates that data. For example, atmospheric models used for “data
 206 assimilation” and global numerical weather prediction, generate the full 3D atmospheric state. In
 207 this case, Equation (2) directly connects model outputs to measurements of the atmospheric state
 208 (data). This means that the likelihood (3) is a measure of the “point-wise” model-data mismatch,
 209 e.g., describing the differences between the observations of the atmospheric states and the predictions
 210 of the atmospheric model. Below, we will use Bayesian inversion to connect the outputs of a LES
 211 with a very simple, phenomenological predator-prey model of stratocumulus clouds without an
 212 associated spatial scale. The more common, point-wise definition of a likelihood is thus not useful
 213 for our purposes and we use a “feature-based” approach. The idea is that while a simplified model
 214 may not be able to reproduce the data in their entirety, it may be able to reproduce selected aspects
 215 of the data, see Morzfeld et al. (2018). The selected aspects that *are* reproducible by the model
 216 are called “features”. A feature-based inverse problem thus requires that we define features that are
 217 comparable in the more usual “point-wise” sense.

218 Specifically, we define $\mathcal{F}_{\mathcal{M}}(\boldsymbol{\theta})$ as a function that extracts the feature from the model and denote
 219 by \mathbf{f}_y the feature extracted from the data. Assuming that discrepancies between the model feature
 220 and the data feature can be accounted for by a random variable, we write

$$\mathbf{f}_y = \mathcal{F}_{\mathcal{M}}(\boldsymbol{\theta}) + \boldsymbol{\varepsilon}. \quad (5)$$

221 If $\boldsymbol{\varepsilon}$ is Gaussian distributed with mean zero and covariance \mathbf{R} (with slight abuse of notation because
 222 \mathbf{R} was used above for another covariance matrix), the feature-based likelihood is

$$p_{l,f}(\mathbf{f}_y|\boldsymbol{\theta}) \propto \exp\left(-\frac{1}{2}\|\mathbf{R}^{-1/2}(\mathbf{f}_y - \mathcal{F}_{\mathcal{M}}(\boldsymbol{\theta}))\|^2\right). \quad (6)$$

223 We emphasize that the feature-based likelihood is defined by the Euclidian norm of the differences
 224 of the model feature and the data feature. The feature-based likelihood measures the point-wise
 225 mismatch of the features of model and data in the same way as the “usual” likelihood measures the
 226 point-wise mismatch between the model outputs and the data (see above). Assuming that a prior
 227 $p_0(\boldsymbol{\theta})$ for the model parameters is given, the feature-based posterior distribution is

$$p_f(\boldsymbol{\theta}|\mathbf{f}_y) \propto p_0(\boldsymbol{\theta}) \exp\left(-\frac{1}{2}\|\mathbf{R}^{-1/2}(\mathbf{f}_y - \mathcal{F}_{\mathcal{M}}(\boldsymbol{\theta}))\|^2\right). \quad (7)$$

228 In summary, a model with parameters distributed according to the feature-based posterior, produces
 229 features that are compatible with the features extracted from the data, up to the assumed errors.
 230 We emphasize that the prior has a direct influence on the shape of the posterior distribution, which
 231 is just the product of prior and likelihood. Since parameter estimates are based on the posterior
 232 distribution, a different choice of prior will ultimately result in different parameter estimates.

233 2.5 Markov chain Monte Carlo for the numerical solution of Bayesian inverse 234 problems

235 Monte Carlo methods can be used to numerically implement the (feature-based) Bayesian inversion.
 236 The idea is to draw samples from the posterior distribution in such a way that averages over the
 237 samples converge to expected values with respect to the posterior distribution when the number of
 238 samples, N_e goes to infinity, see, e.g., Chorin and Hald (2013). In this sense, the samples, generated
 239 by the Monte Carlo method, approximate the posterior distribution and can be used for inferences,
 240 e.g., for computing the posterior mean and covariance matrix.

241 We use Markov chain Monte Carlo (MCMC) to draw posterior samples. A MCMC sampler
 242 operates as follows. A sample is proposed by drawing from a proposal distribution and the proposed
 243 sample is accepted with a probability that ensures that the stationary distribution of the Markov
 244 chain is the targeted posterior distribution, see, e.g., Gilks et al. (1996). The various MCMC
 245 samplers in the literature use different proposal mechanisms to speed up convergence, often by
 246 exploring specific characteristics of the sampling problem. If one does not know of a particular
 247 problem structure to exploit, one should use “general purpose” ensemble samplers, e.g., the affine
 248 invariant MCMC ensemble sampler of Goodman and Weare (2010) or the t-walk of Christen et al.
 249 (2010). These samplers are known to be effective for low-dimensional, nonlinear/non-Gaussian
 250 problems and efficient implementations are also available.

251 To assess the accuracy of the MCMC solution one computes the integrated auto-correlation time
 252 (IACT), see, e.g., Sokal (1996); Wolff (2004). The idea is that, while MCMC samples are generally
 253 not independent, one can estimate an effective number of independent samples by

$$N_{s,\text{eff}} = \frac{N_s}{\text{IACT}}, \quad (8)$$

254 where N_s is the number of samples from the MCMC sampler. The reasoning is that if one has, e.g.,
 255 10^6 samples, and one has computed IACTs of a few hundred, then one should expect an accuracy
 256 that is comparable to that computed with thousands of independent samples.

257 3 Feature-based Bayesian inversion of the LES

258 The KTF17 model parameters are the carrying capacity H_0 , the delay T , the characteristic time
 259 τ and the scaling factor α . We combine these four parameters in the parameter vector $\boldsymbol{\theta} =$
 260 $[H_0, \tau, T, \alpha]^T$. Our goal is to compute the model parameters $\boldsymbol{\theta}$ by a feature-based inversion of
 261 the LES output. As described in Section 2.4, a feature-based inversion requires that we define a
 262 prior distribution and a feature-based likelihood. We now describe in detail how these distributions
 263 are constructed. The feature-based posterior follows from these two distributions and is used for
 264 inferences, numerically implemented by MCMC.

265 3.1 Prior distribution

266 The prior distribution describes our a priori knowledge of the KTF17 model parameters. We define
 267 this prior to be a uniform distribution over the set of parameters that are (i) physically relevant
 268 (positive); and (ii) lead to physically relevant limit cycles in KTF17. All parameters that satisfy
 269 these conditions, receive the same nonzero prior probability while all other parameters receive
 270 zero prior probability. Thus, a parameter vector $\boldsymbol{\theta} = [H_0, \tau, T, \alpha]^T$ must satisfy the following four
 271 conditions in order to receive non-zero prior probability.

- 272 1. All four model parameters must be positive.
- 273 2. The characteristic time to reach carrying capacity is longer than the delay time.
- 274 3. The parameter vector must produce solutions that are limit cycles.
- 275 4. Cloud depth must be positive.

276 For condition 3, we rely on the linear stability analysis in Koren et al. (2017). The parameters that
 277 lead to limit cycles in KTF17 are characterized by the real part of a dimensionless parameter β
 278 being positive. Here,

$$\beta = \frac{\tau}{T} W \left(-2 \left[\sqrt{\frac{1}{\mu} + \frac{1}{4}} - \frac{1}{2} \right] \frac{T}{\tau} \exp \left[\frac{T}{\tau} \right] \right) - 1, \quad (9)$$

279 where $\mu = \sqrt{N}/(\alpha\tau H_0)$ and $W(\cdot)$ is the Lambert-W function. In other words, limit cycles occur
 280 only if $\text{Re}(\beta) > 0$. Condition 4, i.e., checking for negative cloud depth, requires a simulation. For a
 281 given $\boldsymbol{\theta}$, we solve KTF17 numerically and if we detect negative cloud depth, the parameter vector
 282 receives zero prior probability. To streamline computations, we check for negative cloud depth after
 283 checking conditions 1-3.

284 The prior is illustrated in terms of a “triangle plot” in the left panels of Figure 3. A triangle
 285 plot contains histograms of all one and two-dimensional marginals of a given distribution, arranged
 286 in the form of a triangle; each marginal is normalized so that the integral (area under the graph)
 287 is equal to one. A triangle plot is, thus, a qualitative tool that illustrates regions in parameter
 288 space that receive a large probability. Recall that the prior contains the information we have about
 289 model parameters before the data are taken into account. Per our construction of the prior, this
 290 means that a triangle plot of the prior illustrates regions in parameter space that lead to physically
 291 relevant limit cycles of cloud depth.

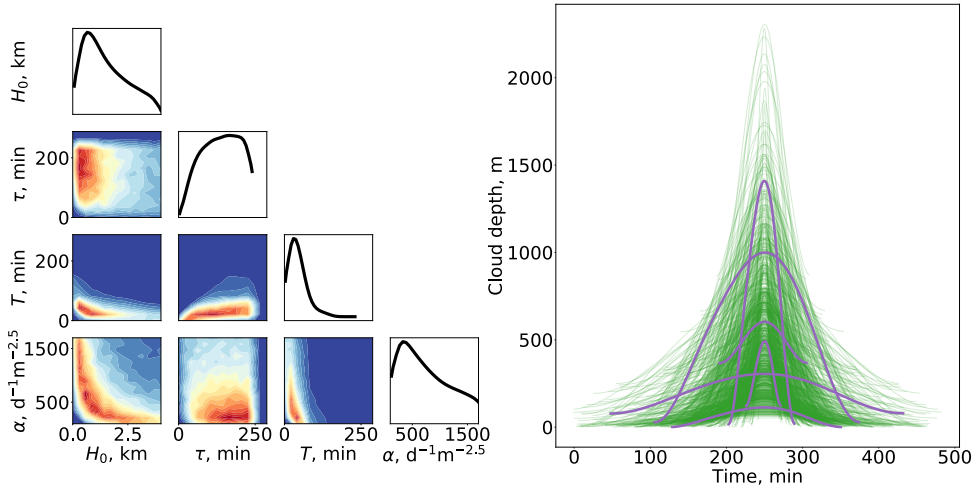


Figure 3: Left: Triangle plot of 10^5 samples of the prior distribution. Blue indicates a low probability while red indicates a high probability. Right: 10^3 limit cycles of KTF17 corresponding to 10^3 parameter vectors drawn at random from the prior. The cycles are aligned to reach their peak depths at the same time. Five examples of cloud cycles are highlighted in purple.

292 Generating the triangle plot requires that we draw samples from the prior which we do via
 293 “importance sampling” with a proposal distribution that is uniformly distributed over the four-
 dimensional hyper-cube defined by the lower and upper parameter bounds listed in Table 1 (for

	H_0 , m	τ , min	T , min	α , $\text{days}^{-1}\text{m}^{-2.5}$
Lower bound	0	0	0	100
Upper bound	4000	288	288	2000
Prior mean	1650	137	43	836
Prior std. dev.	1067	61	27	495

Table 1: Mean and standard deviations computed from 10^5 samples of the prior.

294 more details about importance sampling, see, e.g., Owen (2013); Chorin and Hald (2013)). The
 295 samples that constitute the triangle plot can also be used to compute prior means and standard
 296 deviations, listed in Table 1. We note that the standard deviations are between 40%-60% of the
 297 corresponding mean values, which indicates that the prior is “broad”, i.e., large parts of the parameter
 298 space receive non-zero prior probability.

299 The “broadness” of the prior is further illustrated in the right panel of Figure 3, which shows one
 300 period of 10^3 limit cycles of KTF17 corresponding to 10^3 prior samples of the prior (see Section 3.2
 301 for details of how we compute these limit cycles). The limit cycles are arranged so that their maxima
 302 occur at the same instant. We observe a large variance in the period and amplitude of the cloud
 303 cycles. This means in particular that, a priori, we do not know the typical period or amplitude of a
 304 cloud depth cycle. The goal of a Bayesian inversion is to refine the prior distribution to a posterior
 305 distribution, which reduces variations in the cloud cycles via reducing variance in the parameters;
 306 the reduction of variance of the parameters is achieved by taking the LES into account.
 307

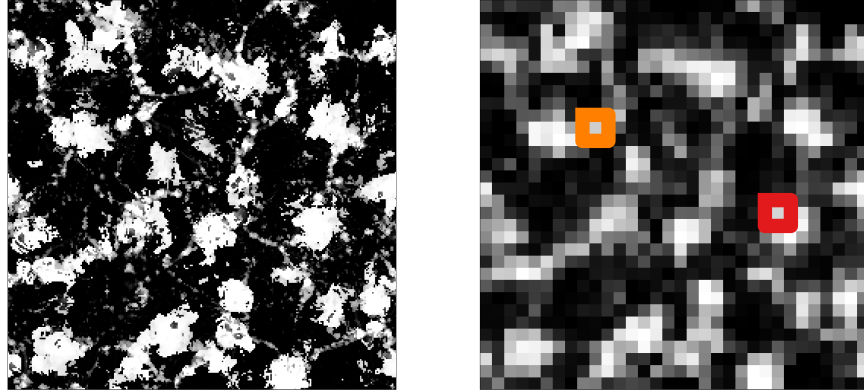


Figure 4: 2D cloud depth field at $t = 4$ hrs at full resolution (256×256 , left) and spatially averaged cloud depth (32×32 , right). Time series of cloud depth for the locations encircled in red and orange are shown in Figure 5.

308 3.2 Feature-based likelihood

309 A feature-based likelihood requires that we define features of the model that can be compared
 310 to features extracted from the data. We now describe how we construct these features and an
 311 associated Gaussian error model.

312 3.2.1 Data feature

313 The data-feature is derived from the time varying 2D cloud depth field of the LES which defines
 314 256×256 time series of cloud depth at each grid point (with no advection present). These time
 315 series, however, are noisy. To reduce the effects of this noise, we spatially average the 2D cloud depth
 316 field over small, square “tiles” that contain a few grid points. We average cloud depth only over
 317 regions where cloud exists, which we define by a positive integral of the liquid water content over the
 318 depth of the cloud (liquid water path), taken from the LES. We considered several tile sizes for the
 319 averaging and settled on tiles containing 8×8 grid points (see also Section 4.1). With a horizontal
 320 grid spacing of 200 m, this results in a “filter” length of about 1,600 m, which is large enough
 321 to smooth out noise, but retains the main aspects of the cellular structure. The full resolution
 322 (256×256) and the spatially averaged (32×32) cloud depth fields are illustrated in Figure 4.

323 The spatial averaging yields 1024 time series of cloud depth, H , over 7.5 hrs. We extract cycles
 324 of growth and decay from these time series as follows. We first apply a temporal smoothing by
 325 applying a Gaussian filter with a standard deviation of 10 minutes. We then compute local extrema
 326 of the filtered time series via finite differencing. Two consecutive local minima define one cycle and
 327 each cycle (without temporal smoothing) is stored. With this procedure, we extract 297 cycles from
 328 the LES.

329 The procedure of the feature extraction is illustrated in Figure 5. Panels (a) and (b) show H ,
 330 after temporal and spatial smoothing, at the locations encircled in red and orange in Figure 4.
 331 Also shown are the extracted cycles (without temporal smoothing). The 297 cycles we compute are
 332 shown in light blue in panel (c); the four cycles, shown in panels (a) and (b), are also shown (in
 333 thicker purple, pink, brown and yellow lines). We align all cycles so that they reach their peaks at
 334 the same instant and pad shorter cycles with zeros, so that all cycles have a duration of 270 minutes
 335 (see also Section 4.1). The feature \mathbf{f}_y is the average of the 297 cycles, shown as a thick dark blue
 336 line in panel (c).

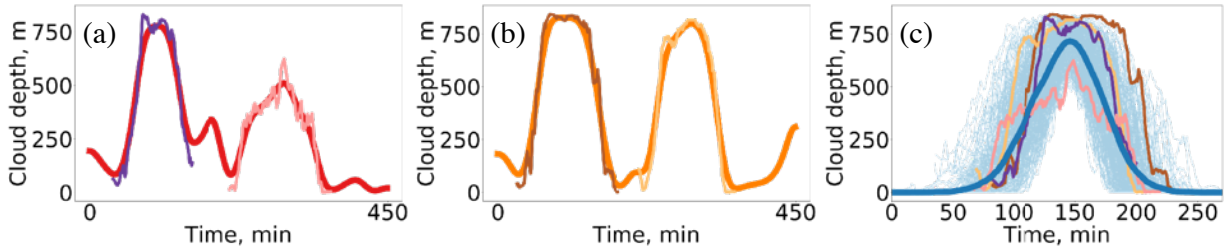


Figure 5: (a) Cloud depth time series after temporal smoothing (red) for the location encircled in red in the right panel of Figure 4. Shown in purple and pink are the two cycles extracted from this time series (without temporal smoothing). (b) Cloud depth time series after temporal smoothing (orange) for the location encircled in orange in the right panel of Figure 4. Shown in brown and yellow are the two cycles extracted from this time series (without temporal smoothing). (c) 297 cycles, extracted from the LES (without temporal smoothing), are shown in light blue. The cloud cycles from panels (a) and (b) are shown in a thicker purple, pink, brown and yellow lines. The dark blue line is the average of the 297 cycles.

3.2.2 Model feature

The model-feature is defined as one limit cycle of KTF17. The limit cycle and the time needed to reach it depend on the value of the model parameters and the initial condition. During the feature-based Bayesian inversion, implemented by an MCMC sampler (see below), the initial conditions are fixed, but we need to find limit cycles corresponding to different parameter values (all with non-zero prior probability).

To robustly compute limit cycles we use the following iterative scheme. We first solve KTF17 numerically for one day (the initial condition is $H(t) = 0.1$ m for $t \leq 0$) and approximate the time derivative of $H(t)$ by finite differences to find the extrema of the cloud depth time series. The time instances of two consecutive local minima define one cycle of growth and decay (note that the data feature is defined in the same way). To check if a limit cycle is reached, we compare the root mean square error (RMSE) between the last two cycles and, if RMSE is less than 1 m, we stop the numerical solution and conclude that the system has reached its limit cycle. Otherwise, we continue the numerical solution of KTF17 for an additional day and, again, find local extrema to define cloud cycles and compute RMSE of the last two cycles. We repeat this process until two consecutive cycles are characterized by an RMSE of less than 1 m. The model-feature is then defined to be the last cycle of the cloud depth time series.

We align the peaks of the model- and data features and modify the model-feature to have the same duration (270 mins) as the data feature. Specifically, if the model feature has a shorter duration than the data feature, we pad the model feature with zeros (symmetrically before and after its peak). If the model feature is longer than the data feature, we truncate it (symmetrically before and after its peak).

Finally, we note that we are not aware of a proof that KTF17 has only *one* limit cycle for a given set of parameters with non-zero prior probability. Extensive numerical experiments, however, suggest that this is indeed the case. In particular, we performed a large number of simulations for several parameter vectors, drawn from the prior, starting at different initial conditions conditions $0 < H(0) < 500$ m (with $H(t) = H(0)$ for $t < 0$) and, for each parameter vector, found only one limit cycle, independent of the initial conditions.

365 **3.2.3 Gaussian error model**

366 To finish the construction of the feature-based likelihood we need to define the errors $\boldsymbol{\varepsilon}$ in Equa-
 367 tion (5). As is customary, we assume a Gaussian distribution with a mean of zero. The covariance
 368 matrix that defines the error model is computed based on the variations of the 297 cloud cycles
 369 extracted from the LES. Specifically, we define the covariance \mathbf{P} as the sample covariance of the
 370 297 cycles and then choose the covariance \mathbf{R} of $\boldsymbol{\varepsilon}$ in (5) as

$$\mathbf{R} = \mathbf{P} + \sigma^2 \mathbf{I}, \quad (10)$$

371 where \mathbf{I} is the identity matrix and $\sigma = 100$ m. Note that \mathbf{P} , \mathbf{R} and \mathbf{I} are matrices of size 270×270 ,
 372 because each (padded) cloud cycle has a duration of 270 mins and the time step is one minute. We
 373 use an additive “inflation” of the covariance \mathbf{P} because the padding leads to small variances at the
 374 beginning and end of the 270 min time interval. We will assess, in hindsight, our assumptions about
 375 errors in the features as well as how the padding with zeros affects the results in Section 4.

376 Each element of Equation (5) is now defined, which implies the feature-based likelihood by (6).
 377 Together with the prior, the feature-based likelihood defines the feature-based posterior, which can
 378 be written as

$$p_f(\boldsymbol{\theta}|\mathbf{f}_y) \propto \begin{cases} 0 & \text{if } p_0(\boldsymbol{\theta}) = 0, \\ \exp\left(-\frac{1}{2}\|\mathbf{R}^{-1/2}(\mathbf{f}_y - \mathcal{F}_{\mathcal{M}}(\boldsymbol{\theta}))\|^2\right) & \text{otherwise,} \end{cases} \quad (11)$$

379 where \mathbf{R} , \mathbf{f}_y and $\mathcal{F}_{\mathcal{M}}(\boldsymbol{\theta})$ are as above.

380 **3.3 Numerical solution by MCMC**

381 We use the python implementation of the t-walk (see <https://www.cimat.mx/jac/twalk/>) and the
 382 python implementation “emcee” of the affine invariant ensemble sampler (Foreman-Mackey et al.,
 383 2013). Below we only show results obtained by emcee, but results obtained by the t-walk are
 384 qualitatively and quantitatively similar. The emcee sampler requires an ensemble of N_e “walkers”,
 385 where

$$N_e \geq 2 \times (\text{number of model parameters}) = 8. \quad (12)$$

386 We chose an ensemble size of $N_e = 20$, because larger ensemble sizes are preferable (Foreman-
 387 Mackey et al., 2013). The initial ensemble is generated as follows. We draw 10^3 samples from the
 388 prior distribution and, for each one, evaluate (7), which is proportional to the posterior probability.
 389 The 20 samples with the highest values, which also correspond to the samples with the highest
 390 posterior probabilities, are the initial ensemble used in emcee.

391 Our code can be found at <https://github.com/SpenceLunderman/LMGF20> and can generate
 392 10^5 samples in about 10 hrs and 10^6 samples in about 4 days (on a single core). For the results
 393 shown below, we discard the first N_{discard} samples as “burn-in”, where $N_{\text{discard}} = 5 \cdot \max \text{IACT}$, and
 394 $\max \text{IACT}$ is the largest IACT of the four parameters. Based on $2 \cdot 10^6$ samples, we compute IACTs
 395 of a few hundred (see below), which indicates that the number of samples we generate is sufficiently
 396 large (accuracy comparable to thousands of independent samples).

397 **4 Results and discussion**

398 We perform the feature-based inversion, as described above, using a constant droplet concentration
 399 of $N = 25 \text{ cm}^{-3}$, which is the time-average of N during the 7.5 hrs of simulation considered. In this
 400 context, it is important to realize that the effect of a varying N over the range encountered in the
 401 LES has a minor effect. The reason is that Equation (1) implies that changes in N result in a scaling

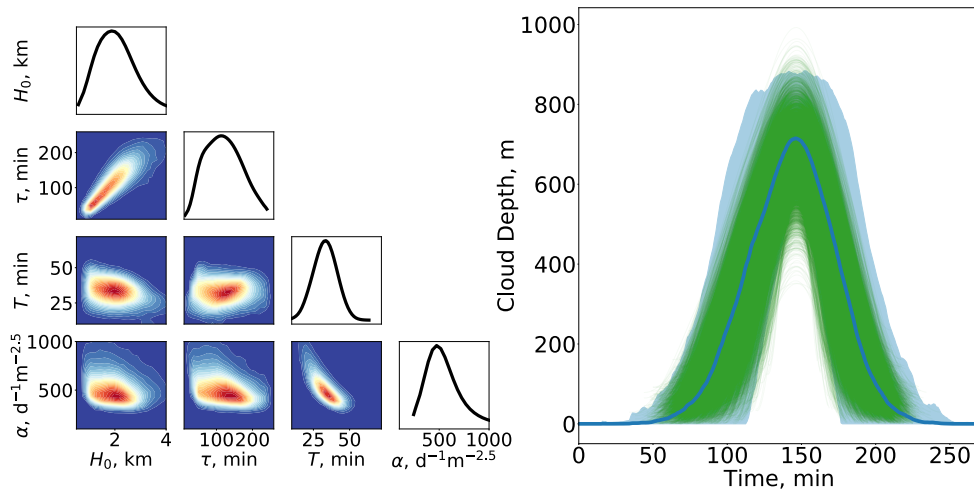


Figure 6: Left: Triangle plot of the posterior distribution ($2 \cdot 10^6$ samples). Right: Shown in green are the limit cycles of KTF17 corresponding to 10^4 parameter vectors drawn at random from the posterior. The LES feature (average of 297 LES cloud cycles) is shown as a dark blue line. The light blue shaded region represents two sample standard deviations of the cloud cycles at each time instant (representing variations in the cloud cycles extracted from the LES).

of α with the square root of N , but all other parameters are independent of the value of N . In particular, if α_0 is estimated by assuming $N = N_0$, then setting $N \rightarrow N_1$ results in $\alpha_1 = \alpha \sqrt{N_1/N_0}$.

The results of the feature-based inversion, based on an MCMC chain with $2 \cdot 10^6$ samples, are illustrated in Figure 6. The left panel shows a triangle plot of the posterior samples, obtained via the MCMC, and the right panel shows 10^4 limit cycles of KTF17, corresponding to 10^4 parameter vectors drawn at random from the posterior. Also shown are the LES feature and the variations in the cloud cycles extracted from the LES. This figure should be compared to Figure 3, which shows the same information *before* the Bayesian inversion, i.e., based on the prior distribution. We note that the posterior distribution is more sharply peaked than the prior (note the different axes in the triangle plots of Figures 3 and 6), which indicates that the LES derived feature indeed constrains all four parameters of KTF17.

The sharpening of the prior to a feature-based posterior distribution can also be seen by computing the sample mean and sample standard deviations, listed in Table 2. We note a shift in the

	H_0 , m		τ , min		T , min		α , $\text{days}^{-1}\text{m}^{-2.5}$	
	Prior	Posterior	Prior	Posterior	Prior	Posterior	Prior	Posterior
Mean	1650	2063	137	120	43	33	836	548
Std.	1067	722	61	48	27	7	495	176
MAP	-	2062	-	131	-	36	-	450

Table 2: Mean and standard deviations of the prior and posterior distributions. The MAP of the posterior is also listed. Posterior quantities are computed from a MCMC chain with $2 \cdot 10^6$ samples; prior quantities are computed from 10^5 samples of the prior.

sample mean and a reduction in sample standard deviations from the prior to posterior distribution. Table 2 further lists the maximum a posteriori (MAP) estimates, i.e., the sample with the largest

417 posterior probability ¹. We note that the MAP and mean are not equal, which indicates that the
 418 posterior distribution is not nearly Gaussian. In this context, it is also important to realize that the
 419 posterior mean is *not* a posterior sample, i.e., its posterior probability can be zero (because it may
 420 not satisfy all four prior constraints). For this reason, the MAP may be a more useful estimate of
 421 the KTF17 parameters than the posterior mean.

422 The left panel of Figure 6 illustrates that cycles of KTF17, obtained by numerical solution of
 423 KTF17 with parameters sampled from the posterior, are well within the variations of the cloud
 424 cycles extracted from the LES. This indicates that our error model and the error covariance matrix
 425 \mathbf{R} are reasonable. Here, we tuned, to some extent, the additive inflation defined by σ in (10). Recall
 426 that error models are notoriously difficult to come by because error models represent “what we do
 427 not know” about the system. Our approach here is to introduce a tunable covariance inflation factor,
 428 σ , that is selected so that the posterior uncertainties, as illustrated by the trajectory ensemble in
 429 the right panel of Figure 6, are reasonable, and within the expected uncertainties, derived directly
 430 from the LES.

431 We can use the results of the feature-based inversion to investigate if the cycles of KTF17 have
 432 similar properties as the cycles extracted from the LES. Specifically, we can consider the period,
 433 amplitude, and growth and decay times of the KTF17 and LES derived cycles. Here, the period
 434 is the duration of the cloud cycle (without zero padding); the amplitude is the difference between
 435 the maximum and minimum cloud depth reached during a cycle ². The cycle growth time describes
 436 how long it takes a cloud to build up to its maximum cloud depth, and the decay time describes
 437 how long it takes to decay from maximum cloud depth to its minimum (equivalently, the decay time
 438 is equal to the period minus the growth time). These four properties are computed for each cloud
 439 cycle extracted from the LES and for 10^4 KTF17 limit cycles, defined by parameters that are drawn
 440 from the posterior distribution. The means and standard deviations of the four cycle properties
 are listed in Table 3. We note that the mean of each cycle property, computed from KTF17, is

	Period, min		Amplitude, m		Growth time, min		Decay time, min	
	LES	KTF17	LES	KTF17	LES	KTF17	LES	KTF17
Mean	137	119	619	591	69	66	69	55
Std. Dev.	23	26	142	102	23	15	19	12

Table 3: Mean and standard deviations of cloud cycle properties of the LES and KTF17. LES results are computed from 297 cycles and KTF17 results are computed from 10^4 simulations with parameters drawn from the posterior distribution.

441 within one standard deviation of the mean of the corresponding property computed from the LES.
 442 Moreover, the standard deviations of the LES and KTF17 cycle properties are also comparable,
 443 which suggests an overall good “fit” of KTF17 to the LES in terms of these cycle properties.
 444

445 To report on the statistical accuracy of the MCMC solution, we list the IACTs, estimated from
 446 the $2 \cdot 10^6$ samples, of all four parameters in Table 4. The IACTs are less than 10^3 , which indicates
 447 that the number of samples is sufficient to accurately compute posterior means, standard deviations

¹It is important to remember that marginal distributions, shown in the form of histograms in the triangle plots, are not “projections” of the multivariate probability distribution. For this reason, the maxima of the posterior marginals (histograms) do not correspond to the mode of the multivariate posterior distribution (MAP).

²We emphasize that the blue line, shown in Figure 6, is the average of the LES cycles, but taking into account the zero padding, and stitching the cloud cycles together at their maximum value. This means that the maximum value of the blue line in Figure 6 equals the average maximum cloud depth over all cycles, which is different from the average amplitude in Table 3. The same reasoning explains why the average amplitude of KTF17, reported in Table 3, is different from what one might expect by visually taking the average of the green lines in Figure 6.

H_0 , m	τ , min	T , min	α , days ⁻¹ m ^{-2.5}
620	326	539	665

Table 4: Integrated autocorrelation times (computed from the $2 \cdot 10^6$ samples).

448 and the MAP, with an effective sample size in the thousands.

449 4.1 Robustness of the LES feature

450 The computational framework we describe, and in particular the construction of the LES feature,
 451 relies on several assumptions and modeling choices. The Bayesian approach and MCMC implemen-
 452 tation allow us to investigate, numerically, the validity of our assumptions and choices. We already
 453 described the effects of the error model and our choice of additive covariance inflation (see Figure 6).
 454 We now investigate the robustness of the LES feature to two other modeling choices: the spatial
 455 smoothing and the zero-padding of the cloud cycles (see Section 3.2.1).

456 4.1.1 Robustness to spatial smoothing

457 While it is difficult to determine the precise amount of spatial smoothing, it is clear that (i) smooth-
 458 ing is necessary, or else the cloud depth time series are too noisy; and (ii) that there is a maximum
 459 amount of smoothing that should not be exceeded, or else the effects of cloud entities are averaged
 460 out. We investigate this issue by performing the feature-based Bayesian inversion for three spatial
 461 averages over “tiles” consisting of 4×4 , 8×8 and 16×16 grid points respectively. With each spatial
 462 averaging, we compute the data-feature and perform the Bayesian inversion via MCMC, generating
 463 $2 \cdot 10^6$ samples in each configuration. In all three cases, the prior distribution is the same as above,
 464 because the prior is independent of the definition of features, or, equivalently, the likelihood. We also
 465 keep all other aspects (covariance inflation, temporal smoothing etc.), that define the data-feature,
 466 as above.

467 Table 5 lists the posterior mean, standard deviation and MAP estimates for three spatial smooth-
 ings, computed from three MCMC runs with $2 \cdot 10^6$ samples. We note that the parameter estimates

Tile width	H_0 , m			τ , min			T , min			α , days ⁻¹ m ^{-2.5}		
	4	8	16	4	8	16	4	8	16	4	8	16
Mean	2344	2063	1776	114	120	141	29	33	41	560	548	458
Std.	989	722	544	48	48	49	7	7	6	183	176	83
MAP	2147	2062	2215	119	131	188	34	36	42	453	450	414

Table 5: Posterior means, standard deviations, and MAP estimates for the four parameters of KTF17 and for the three configurations which differ in their spatial smoothing of the LES cloud depth field. Posterior means, the MAP, and standard deviations are computed from the MCMC chain with $2 \cdot 10^6$ samples.

468 for the three configurations are within a standard deviation of each other, independently of which
 469 standard deviation one choses to use. The only exception is the parameter T , where the estimates
 470 for the 16×16 case are within two standard deviations of the 4×4 or 8×8 scenario. A smoothing
 471 over 16×16 grid points may, therefore, be labeled as excessive.
 472

473 Nonetheless, averaging over tiles of size 4×4 or 8×8 gives nearly identical results, which indicates
 474 some robustness of our approach with respect to spatial smoothing. We emphasize, however, that

475 a significantly larger amount of smoothing (tiles consisting of more than 16×16 grid points) does
 476 not lead to reasonable parameter estimates because the effects of cloud entities are averaged out.

477 4.1.2 Robustness to padding of LES cycles

478 In the construction of the LES feature, cycles are aligned at their peaks of cloud depth. The cycles
 479 are then “padded with zeros” so that all cycles have the same duration (270 min). The LES feature
 480 is simply the average of the padded cycles. Below, we call this construction “Version (a)”. We now
 481 investigate the consistency of the parameter estimation results when we choose another method to
 482 derive the LES feature that does not make use of zero padding.

483 In “Version (b)”, we again align all cloud cycles at their peaks, but rather than padding with
 484 zeros, we average only those cycles that “exist”, i.e., which have non-zero cloud depth at a given time
 485 instant. We further exclude all instances where less than 10 cycles exist. The error covariance of ϵ
 486 for Version (b) is computed in the same way as in Version (a). Figure 7 illustrates the LES feature of
 487 versions (a) and (b). Note that the duration of the average in Version (b) is shorter than in Version
 488 (a) because we only consider instances when at least 10 cycles are non-zero and longer cycles occur
 489 less frequently. We further note that near the peak, these two versions are equal because, at peak
 490 times, zero padding in Version (a) has no effect and no cycles are excluded in Version (b) because
 491 more than 10 cycles exist.

492 We perform a feature-based Bayesian inversion for LES features constructed using versions (a)
 and (b) and, as before, generate $2 \cdot 10^6$ samples by MCMC. Results are shown in Table 6.

	H_0 , m		τ , min		T , min		α , days ⁻¹ m ^{-2.5}	
	Version (a)	Version (b)	V. (a)	V. (b)	V. (a)	V. (b)	V. (a)	V. (b)
Mean	2063	2008	120	126	33	35	548	526
Std.	722	684	48	50	7	9	176	180
MAP	2062	2321	131	164	36	38	450	430

Table 6: Posterior means, standard deviations and MAP estimates for the four parameters of KTF17 and for the two configurations which differ in their calculation of the LES feature. Version (a) and Version (b) correspond to the two LES features shown in Figure 7. Posterior means, the MAP and standard deviations are computed from the MCMC chain with $2 \cdot 10^6$ samples.

493 We note that the parameter estimates resulting from versions (a) and (b) are not significantly
 494 different. The reason is that most KTF17 cycles occur between 50 and 200 minutes (see Figure 6),
 495 i.e., when the two LES features of versions (a) and (b) are similar. The similarities between these
 496 two posterior distributions can also be seen in the marginal distributions in Figure 8. The left panel
 497 shows a triangle plot of the posterior distribution of Version (a) and the left panel shows a triangle
 498 plot of the posterior distribution of Version (b). In both panels, the plots on the diagonals show the
 499 one-dimensional marginal distributions of both posteriors in black (Version (a)) and blue (Version
 500 (b)). In summary, the similarity in the parameter estimates and posterior distributions of Versions
 501 (a) and (b) suggests that estimation framework we describe is robust to small changes in the details
 502 of how one calculates the data feature.
 503

504 4.2 Studying changes in cloud system morphology

505 The Bayesian inversion and the KTF17 model will prove useful if one can map meteorological
 506 conditions to changes in the parameters of KTF17. We illustrate how to do this with a simple
 507 example in which we start to investigate the effects of large-scale changes within the cloud field on

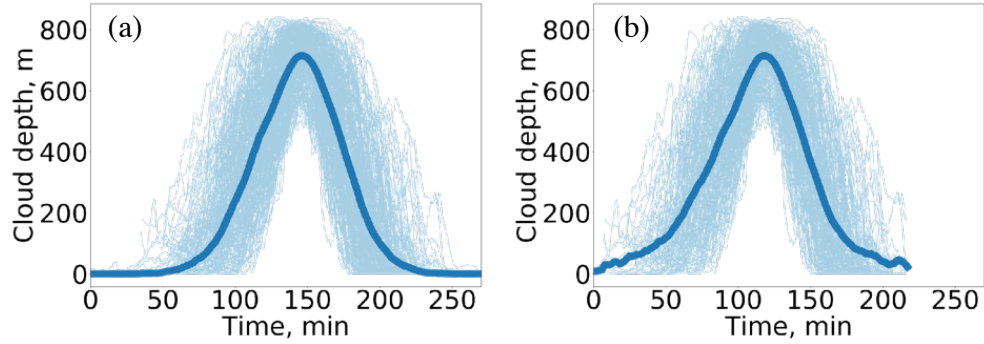


Figure 7: Cloud cycles and data feature of Version (a) (left) and Version (b) (right). Light blue: LES cycles. Thick blue: LES feature.

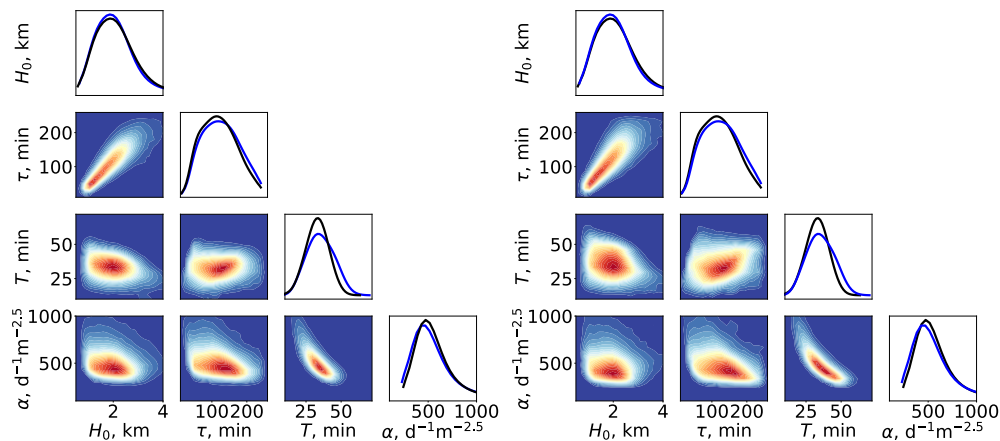


Figure 8: Left: triangle plot of the posterior distribution of Version (a). Right: triangle plot of the posterior distribution of Version (b). The diagonal plots of each panel show the one-dimensional marginals of both distributions (in black for Version (a), in blue for Version (b)). All plots are based on $2 \cdot 10^6$ MCMC samples.

508 the parameters of KTF17. We base this investigation on only one LES, which represents one cloud
 509 system and, for that reason, our results and conclusion are limited.

510 We note that the cloud system undergoes a change in its morphology from a relatively dense
 511 cloud configuration with a higher average cloud fraction to a sparse coverage with a lower average
 512 cloud fraction (see Figure 1). During this transition, the droplet concentration also decreases (see
 513 Figure 2). The transition occurs roughly at the 3.5 hour mark and aligns with a change in the
 514 thickness of the boundary layer, whose thickness increases until about 3.5 hours, and then decreases.

515 To investigate the effects of the morphological change in the macro-structure of the cloud system
 516 on the parameters of KTF17, we perform two feature-based inversions as follows. We separate
 517 the cloud cycles, extracted from the LES, into two groups: cycles occurring before and after the
 518 transition from the dense to the sparse cloud cover, i.e., before or after 3.5 hr. For example, the
 519 cloud cycles shown in purple and brown in panels (a) and (b) of Figure 5 occur before the transition
 520 (dense phase), but the cycles shown in pink and yellow occur after the transition (sparse phase).
 521 In this way, we obtain 166 cycles during the dense phase and 131 during the sparse phase, shown
 522 along with their averages (using zero-padding) in Figure 9.

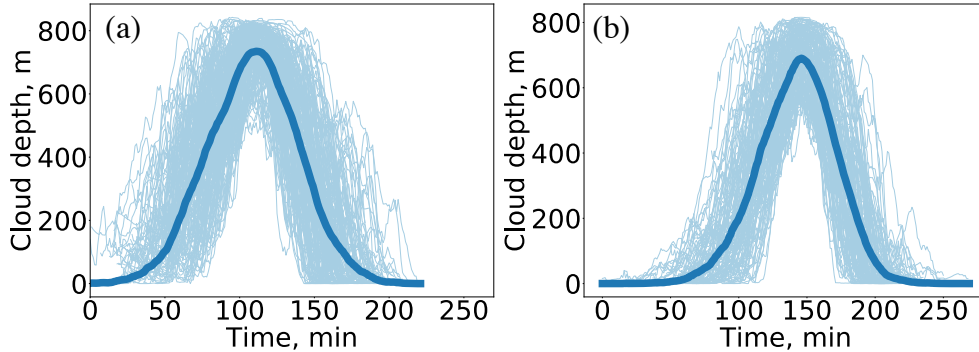


Figure 9: Cloud cycles and data feature for the dense (a) and sparse phases (b). Light blue: LES cycles. Thick blue: LES feature.

523 We compute data-features separately for the dense and sparse phases using the techniques
 524 described above (using the default spatial smoothing over tiles consisting of 8×8 grid points and
 525 Version (a), i.e., zero padding of the cycles). In this way, we define feature-based likelihoods for
 526 the dense and sparse phases. We use the same prior for the dense and sparse phases to define
 527 two posterior distributions. We assign the time average of the droplet concentration in Figure 2,
 528 computed separately over the dense and sparse phases, as the values used for N in the Bayesian
 529 inversion. Specifically, we chose $N = 31 \text{ cm}^{-3}$ for the dense phase and $N = 20 \text{ cm}^{-3}$ for the sparse
 530 phase. As before, we use the MCMC sampler to draw $2 \cdot 10^6$ samples from the posterior distributions
 531 associated with the dense and sparse phases.

Table 7 lists parameter estimation results for the two dense and sparse phases. We note that

	H_0 , m		τ , min		T , min		α , $\text{days}^{-1}\text{m}^{-2.5}$	
	Dense	Sparse	Dense	Sparse	Dense	Sparse	Dense	Sparse
Mean.	2028	1886	122	110	36	32	525	535
Std.	615	616	45	44	6	7	117	166
MAP	2112	2408	130	165	36	36	483	405

Table 7: Maximum a posteriori (MAP) estimate, posterior mean and posterior standard deviation for the dense and sparse phases, computed from MCMC chains with $2 \cdot 10^6$ samples.

532 the parameter estimates (posterior mean and MAP) are within one standard deviation of each
 533 other. Furthermore, the parameter estimates listed in Table 7 are comparable with the parameters
 534 in Table 5, which are estimated based on *all* cloud cycles extracted from the LES (i.e., cycles in
 535 dense and sparse configurations). Similarities and differences in the parameter estimates can also
 536 be illustrated by triangle plots of the two posterior distributions, shown in Figure 10. The left panel
 537 shows the posterior distribution associated with the dense phase; the right panel shows the posterior
 538 distribution associated with the sparse phase. It is apparent that the posterior distributions are
 539 quite similar, but it is also apparent that there are differences, especially in the delay T and the
 540 scaling factor α .
 541

542 It is difficult to determine whether or not the differences in the parameter estimates are sig-
 543 nificant. Taking into account the standard deviations as an indicator of uncertainty, one may be
 544 tempted to conclude that the differences are not significant. One can study this further by compar-
 545 ing the differences in parameter estimates induced by the dense and sparse phases, with differences
 546 induced by variations in the smoothing or paddings. Figure 11 illustrates this point and shows 1D

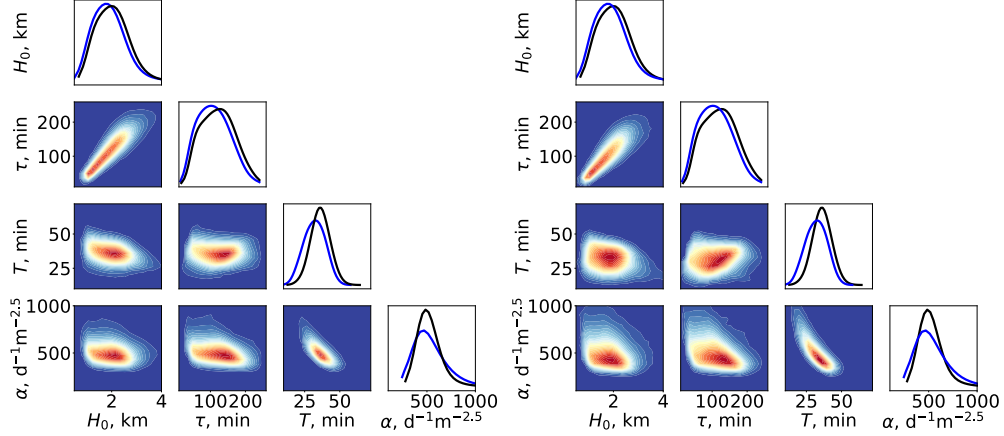


Figure 10: Left: triangle plot of the posterior distribution associated with the dense phase. Right: triangle plot of the posterior distribution associated with the sparse phase. The diagonal plots of each panel show the one-dimensional marginals of both distributions (in black for the dense, in blue for the sparse phase). All plots are based on $2 \cdot 10^6$ MCMC samples.

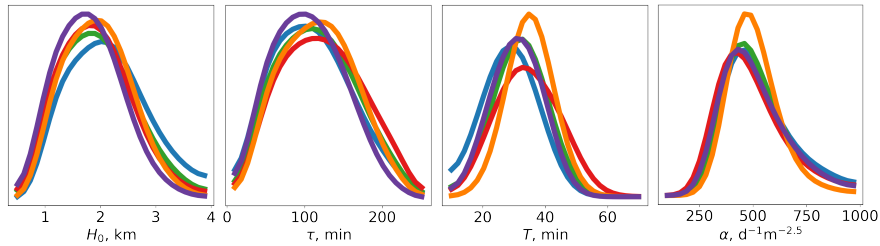


Figure 11: Marginal posterior distributions over the four parameters. Left to right: H_0 , τ , T and α . Green: 8×8 spatial smoothing, zero padding, all cycles. Blue: 4×4 spatial smoothing, zero padding, all cycles. Red: 8×8 spatial smoothing, no padding, all cycles. Orange: 8×8 spatial smoothing, zero padding, dense cycles. Purple: 8×8 spatial smoothing, zero padding, sparse cycles.

547 posterior marginals over the four parameters for five of the cases considered. Three of the cases
 548 (green, blue and red in Figure 11) indicate uncertainty in parameter estimates induced by variations
 549 in the numerical setup. Variation in the posterior distributions indicates the variability one should
 550 expect due to different choices in the numerics. We then overlay the posterior distributions defined
 551 by only the dense or only the sparse phase cycles (orange and purple in Figure 11). The variation of
 552 these distributions indicates variability in the parameter estimates caused by changes in the large
 553 scale structure of the cloud system. We note, as before, the largest differences in the delay T and
 554 the scaling factor α .

555 One can further investigate how differences in the parameter estimates propagate to character-
 556 istics of the cloud cycles, such as their period, amplitude, and growth and decay times (see above
 557 for definitions). We compute the period, amplitude, and growth and decay times based on the LES
 558 for three cases (i) using all cycles; (ii) using only cycles of the dense phase; (iii) using only cycles
 559 of the sparse phase. We then repeat this procedure for the KTF17 model with parameters drawn
 560 from the posterior distributions corresponding to the above three cases. Figure 12 illustrates this
 561 point. Here we plot the average and standard deviation of the cloud cycle properties for the LES
 562 (left) and KTF17 (right) for the three cases; all quantities are scaled by the associated mean value

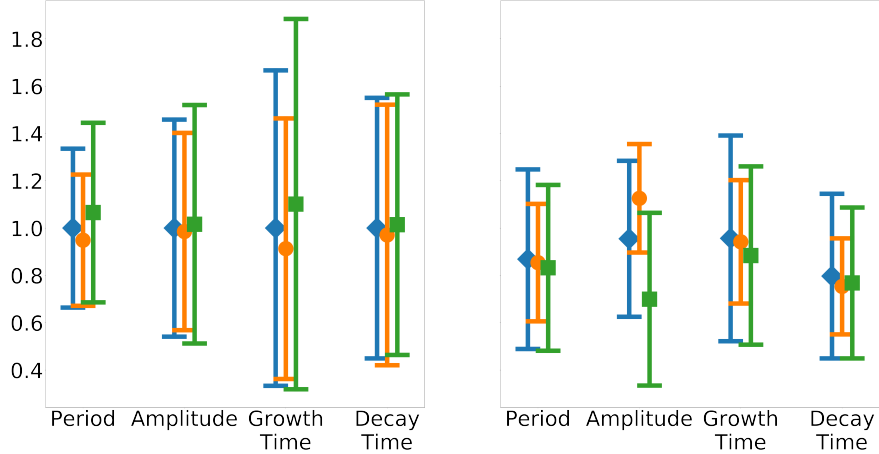


Figure 12: Mean and standard deviation of the period, amplitude, growth time and decay time of cloud cycles. Left: LES. Right: KTF17. Blue diamond – all cycles. Orange circle – dense cycles. Green square – sparse cycles. All quantities are scaled by the average values computed from all cycles of the LES.

563 of the LES case (i). We note that the properties of the LES do not change dramatically when
 564 moving from dense to sparse phases. Moreover, the cycle properties of KTF17 are comparable with
 565 those of the LES, but we observe a larger spread in the amplitude. Since the cycle properties do
 566 not change much during the transition from the dense to the sparse phase, one might expect that
 567 parameters of the KTF17 model should also be largely unaffected by this transition. Taking also the
 568 similarities in the parameter estimates and posterior distributions into account, one might conclude
 569 that the cycles of cloud patches within a cloud system may not necessarily be affected by changes
 570 in the macro-structure of the cloud system. This conclusion, however, is based on a single LES,
 571 which represents a case study with specific large-scale and thermodynamic boundary conditions. It
 572 is conceivable that KTF17 parameters will be sensitive to these boundary conditions.

573 5 Summary and conclusions

574 Stratocumulus clouds are an important part of the Earth system and have a large effect on Earth’s
 575 overall radiative balance and climate. For these reasons, stratocumulus cloud systems are studied
 576 computationally by a hierarchy of models ranging from simplified, phenomenological models to cloud
 577 resolving simulations of the atmosphere. We described a conceptual and computational strategy
 578 for turning a simplified, phenomenological model into a quantitative tool. Specifically, we use the
 579 nonlinear rain equation (KTF17) and estimate its parameters from the outputs of a large eddy
 580 simulation (LES).

581 The main technical difficulty for such a parameter estimation is that the phenomenological model
 582 and the LES operate in vastly different regimes in terms of what the two models are actually capable
 583 of. In particular, the LES has temporal and spatial scales, whereas KTF17 has no associated spatial
 584 scale. We overcame these difficulties by realizing that the KTF17 model produces cycles of cloud
 585 growth and decay that are comparable to cycles within the LES. We use cycles of growth and decay
 586 to define “features” and base the parameter estimation on these features. This includes deriving
 587 error models for the features which in turn allows us to formulate the parameter estimation problem
 588 within the Bayesian framework. The resulting Bayesian inverse problem is solved numerically by a

589 Markov chain Monte Carlo method, which allows us to assess posterior uncertainties.

590 We carefully studied the validity of our assumptions and modeling choices. The error model,
591 which is notoriously difficult to construct because it represents “what we do not know”, was set up to
592 have one tunable parameter (defining an additive covariance inflation). This parameter is tuned so
593 that posterior uncertainties are reasonable and match the variability in the cycles derived from the
594 LES. In addition, we investigated the robustness of our approach to the details of the construction
595 of the features (spatial smoothing of the LES cloud depth fields and zero-padding of resulting
596 cloud cycles). Stringent tests of this type are necessary to show that the estimated parameters are
597 precise enough for drawing conclusions. Our numerical experiments indeed suggest that the KTF17
598 model, with parameters distributed according to the feature-based posterior distribution, is robustly
599 capable of representing cloud cycle properties of a LES.

600 As an illustration of how one may use a simplified model as a quantitative tool, we investigated
601 the sensitivity of the KTF17 parameters to morphological changes within the cloud system simulated
602 by the LES. The system evolves from relatively dense cloud configuration to a sparse coverage (see
603 Figure 1). The KTF17 parameters do not change significantly during the morphological transition
604 of the system, which suggests that cycles of cloud growth and decay of cloud patches may be
605 independent of the large-scale behavior of the system. This result, however, is conditional on the
606 one LES we considered and it is likely that the KTF17 parameters are indeed sensitive to changes
607 in other meteorological conditions, e.g., in the boundary conditions. Future work will explore this
608 idea with a range of LES in different meteorological conditions.

609 Acknowledgments

610 We thank Prof. Joceline Lega of the University of Arizona for interesting and inspiring discussion.
611 GF acknowledges a long collaboration with Ilan Koren on the predator prey model as applied to
612 cloud systems.

613 SL and MM gratefully acknowledge support by the National Science Foundation under grant DMS-
614 1619630. FG acknowledges support by a National Research Council Research Associateship award
615 at the National Oceanic and Atmospheric Administration (NOAA), by the Innovational Research
616 Incentives Scheme Veni of the Netherlands Organisation for Scientific Research and by The Branco
617 Weiss Fellowship – Society in Science, administered by the ETH Zurich.

618 References

- 619 Agee, E. M. (1984). Observations from space and thermal convection: A historical perspective.
620 *Bulletin of the American Meteorological Society*, 65(9):938–949.
- 621 Asch, M., Bocquet, M., and Nodet, M. (2017). *Data Assimilation: Methods, Algorithms, and*
622 *Applications*. SIAM, Philadelphia.
- 623 Boucher, O., Randall, D., Artaxo, P., Bretherton, C., Feingold, G., Forster, P., Kerminen, V.-M.,
624 Kondo, Y., Liao, H., Lohmann, U., Rasch, P., Satheesh, S., Sherwood, S., Stevens, B., and Zhang,
625 X. (2013). Clouds and aerosols. In Stocker, T. F., Qin, D., Plattner, G.-K., Tignor, M., Allen, S.,
626 Boschung, J., Nauels, A., Xia, Y., Bex, V., and Midgley, P., editors, *Climate Change 2013: The*
627 *Physical Science Basis. Contribution of Working Group I to IPCC AR5: Clouds and Aerosols*.
628 Cambridge.

- 629 Chorin, A. and Hald, O. (2013). *Stochastic Tools in Mathematics and Science*. Springer, New York,
630 third edition.
- 631 Christen, J. A., Fox, C., et al. (2010). A general purpose sampling algorithm for continuous distri-
632 butions (the t-walk). *Bayesian Analysis*, 5(2):263–281.
- 633 Feingold, G. and Koren, I. (2013). A model of coupled oscillators applied to the aerosol cloud
634 precipitation system. *Nonlinear Processes in Geophysics*, 20(6):1011–1021.
- 635 Feingold, G., Koren, I., Yamaguchi, T., and Kazil, J. (2015). On the reversibility of transitions
636 between closed and open cellular convection. *Atmospheric Chemistry and Physics*, 15(13):7351–
637 7367.
- 638 Foreman-Mackey, D., Hogg, D. W., Lang, D., and Goodman, J. (2013). Emcee: the MCMC hammer.
639 *Publications of the Astronomical Society of the Pacific*, 125(925):306.
- 640 Gilks, W., Richardson, S., and Spiegelhalter, D. (1996). Introducing Markov chain Monte Carlo. In
641 Gilks, W., Richardson, S., and Spiegelhalter, D., editors, *Markov Chain Monte Carlo in Practice*,
642 chapter 1, pages 1–20. Springer-Science+Business Media.
- 643 Glassmeier, F. and Feingold, G. (2017). Network approach to patterns in stratocumulus clouds.
644 *Proceedings of the National Academy of Sciences*, 114(40):10578–10583.
- 645 Goodman, J. and Weare, J. (2010). Ensemble samplers with affine invariance. *Communications in*
646 *applied mathematics and computational science*, 5(1):65–80.
- 647 Koren, I. and Feingold, G. (2011). Aerosol–cloud–precipitation system as a predator-prey problem.
648 *Proceedings of the National Academy of Sciences*, 108(30):12227–12232.
- 649 Koren, I. and Feingold, G. (2013). Adaptive behavior of marine cellular clouds. *Scientific Reports*,
650 3:2507.
- 651 Koren, I., Tziperman, E., and Feingold, G. (2017). Exploring the nonlinear cloud and rain equation.
652 *Chaos: An Interdisciplinary Journal of Nonlinear Science*, 27(1):013107.
- 653 Maclean, J., Santitissadeekorn, N., and Jones, C. K. (2017). A coherent structure approach for
654 parameter estimation in Lagrangian data assimilation. *Physica D: Nonlinear Phenomena*, 360:36–
655 45.
- 656 Morzfeld, M., Adams, J., Lunderman, S., and Orozco, R. (2018). Feature-based data assimilation
657 in geophysics. *Nonlinear Processes in Geophysics*, 25(2):355–374.
- 658 Myhre, G., Shindell, D., Bréon, F.-M., Collins, W., Fuglestedt, J., Huang, J., Koch, D., Lamarque,
659 J.-F., Lee, D., Mendoza, B., Nakajima, T., Robock, A., Stephens, G., Takemura, T., and Zhang,
660 H. (2013). Anthropogenic and natural radiative forcing. In Stocker, T. F., Qin, D., Plattner,
661 G.-K., Tignor, M., Allen, S., Boschung, J., Nauels, A., Xia, Y., Bex, V., and Midgley, P., editors,
662 *Climate Change 2013: The Physical Science Basis. Contribution of Working Group I to IPCC*
663 *AR5: Anthropogenic and Natural Radiative Forcing*. Cambridge.
- 664 Nober, F. J. and Graf, H. F. (2005). A new convective cloud field model based on principles of
665 self-organization. *Atmospheric Chemistry and Physics*, 5:2749–2759.
- 666 Owen, A. (2013). *Monte Carlo Theory, Methods and Examples*.
667 <https://statweb.stanford.edu/~owen/mc/>.

- 668 Reich, S. and Cotter, C. (2015). *Probabilistic Forecasting and Bayesian Data Assimilation*. Cam-
669 bridge University Press, Cambridge.
- 670 Schneider, T., Teixeira, J., Bretherton, C. S., Brient, F., Pressel, K. G., Schär, C., and Siebesma,
671 A. P. (2017). Climate goals and computing the future of clouds. *Nature Climate Change*, 7(1):3.
- 672 Sokal, A. (1996). Monte Carlo methods in statistical mechanics: Foundations and new algorithms.
673 In C., D.-M., P., C., and A., F., editors, *Functional Integration*, volume 361. NATO ASI Series
674 (Series B: Physics).
- 675 Tarantola, A. (2005). *Inverse Problem Theory and Model Parameter Estimation*. SIAM, Philadel-
676 phia.
- 677 Wolff, U. (2004). Monte Carlo errors with less errors. *Computer Physics Communications*,
678 156(2):143–153.
- 679 Wood, R. (2012). Stratocumulus clouds. *Monthly Weather Review*, 140(8):2373–2423.
- 680 Wood, R. and Hartmann, D. L. (2006). Spatial variability of liquid water path in marine low cloud:
681 The importance of mesoscale cellular convection. *Journal of Climate*, 19(9):1748–1764.
- 682 Yamaguchi, T., Feingold, G., and Kazil, J. (2017). Stratocumulus to cumulus transition by drizzle.
683 *Journal of advances in modeling earth systems*, 9:2333–2349.